Postprint of: Doroszko M., Seweryn A., Numerical modelling of the mesofracture process of sintered 316L steel under tension using microtomography, ENGINEERING FRACTURE MECHANICS, Vol. 255 (2021), 107965-, DOI: 10.1016/j.engfracmech.2021.107965

Numerical modelling of the mesofracture process of sintered 316L steel under tension using microtomography

M. Doroszko [a], *, A. Seweryn [b]

m.doroszko@pb.edu.pl, andrzej.seweryn@pg.edu.pl

[a] Faculty of Mechanical Engineering, Bialystok University of Technology, 45C Wiejska, Bialystok, 15-351, Poland

[b] Faculty of Mechanical Engineering and Ship Technology, Gdańsk University of Technology, 11/12 Gabriela Narutowicza, Gdańsk, 80-233, Poland

ABSTRACT

This paper concerns numerical modelling of the deformation process, taking into account the local fracture of porous 316L sinters at the mesoscopic scale using the finite element method. Calculations are performed with the use of geometrical models, to map the realistic shape of the porous mesostructure of the material, obtained by means of computed microtomography. The microtomographic device has limited and insufficient measurement accuracy for materials such as the porous sinters studied. For this reason, a method to compensate the inaccuracy of mesostructure shape-mapping is used in the numerical modelling of the deformation and fracture process of the material. The normalised Cockroft-Latham ductile fracture criterion is used to model the local fracture process (at the mesostructure level) of porous metal sinters under tension. The paper describes the numerical modelling procedure and the results of the calculations. The influence of the material structure on the meso-scale fracture process is also discussed. The numerical nominal stress-strain curves are compared with the results of experimental testing. The analysis of stress and strain fields and their variability caused by local fracture in the investigated heterogeneous material is also carried out.

Keywords: fracture process, numerical modelling, finite element analysis, microtomography, sintered porous metals

1. Introduction

Porous metallic materials are characterised, inter alia, by a comparatively low relative density while maintaining high stiffness and strength [1]. Nowadays, they are mainly used in the automotive, aviation and medical industries [2–4]. In this paper, porous sinters of 316L steel with various porosities, obtained by powder metallurgy, were used for the research [5,6]. Due to their mechanical properties and corrosion resistance, the sinters investigated are some of those used in the production of implants, especially as a bone substitute material [7,8].

Due to the complicated shapes of the material pores, many different approaches are currently used to take into account the spatial shape of the porous structure in numerical modelling [9]. Some of them assume the generation of a simplified pore network geometry, usually through the use of various types of algorithms [10–14]. The approach of mapping the actual shape of the tested porous structure is increasingly used. In the works of Chawla and Deng [15] and Deng et al. [16], the shape of the porous structure of the material was mapped using a microscope and the cross-section obtained was then used for 2D numerical calculations of the material's strength properties. To map the shape of the spatial structure of porous materials, the serial sectioning method and x-ray computed tomography method are mainly used to obtain images of cross-sections of the investigated materials. The serial sectioning method consists of removing the material layer, then smoothing the surface and recording the cross-section image using, for example, a microscope [17–19]. The number of sections for the 3D reconstruction of the shape of the porous structure depends on the number of material removal and cross-section saving sequences performed. Due to the complexity and time required for this method, its use is significantly limited. Due to the characteristics and limitations of the serial-sectioning method, the method that uses computed microtomography is more often used to map the shape of porous structures. Recently, there have been many studies of heterogeneous materials and numerical modelling of their mechanical properties based on microtomography [20–25]. In the work of Luo et al. [20], the yielding of metal foams under multiaxial loading was analysed. Madej et al. [21] investigated and numerically modelled the properties of sintered metallic materials. The concrete fracture process was also modelled with the use of computer microtomography [22]. In the work of Askari et al. [23], the results of experimental studies and compressive mechanical properties of 3D zirconia scaffolds for bone tissue engineering were analysed. The work by Doroszko and Seweryn [24] concerns the numerical modelling of the compression process and the simultaneous densification of porous sinters of 316L steel. In the work of Ghazi et al. [25], the behaviour of loaded metallic foams (closed cell) was modelled using shell approximation.

The fracture process of metallic porous materials is now a frequently discussed research topic. It is related both to the development of the production technology and the development of computer methods, enabling the analysis of this process. Most of the work is in the field of experimental research [26–30]. Kashef et al. [26] describes the influence of the morphology of titanium foams on their fracture toughness. The work of Liu et al. [27] concerns experimental studies of the deformation and fracture of oriented linear porous metals. In turn, in the articles by Falkowska and Seweryn [28], Falkowska et al. [29] present the results of an analysis of the fracture process of the porous sinters of 316L steel as a result of fatigue loading. In the work of Shevtsova et al. [30], the results of research on the mechanical properties of Ni_3Al–Ni powder mixtures obtained with spark plasma sintering are discussed. Due to the complexity and heterogeneity of porous structures, determining their influence on the process of local fracture and then global failure of the material is a complicated issue. In order to better understand the relationship between the porosity structure of the material and its impact on the fracture and failure processes, numerical modelling and simulation methods are increasingly used, taking into account the shape and morphology of the pores in the material [31–34]. In the work of Kaya et al. [31], damage to individual bridges of sintered steel foam during tension was investigated. The work of Perzyński et al. [32] concerns numerical modelling of the fracture process of two-phase steels. An analysis of closed-cell aluminium foam with crushing behaviour was also performed [33]. The article by Kozma and Zsoldos [34] presents the results of research on the fracture process of syntactic foams.

This paper concerns the numerical modelling of the deformation and fracture process, taking into account the local fracture of porous sinters of 316L steel, using the finite element method. Sinters with various porosity values were used for the investigation. The shape of the porous mesostructure of the materials was included in the numerical calculations using computed microtomography. Micro-CT devices indicate insufficient accuracy of measurement of geometry details (fissures and small pores) of the porous structure of the studied sinters [35]. The lack of mapping results in the overestimation of the obtained nominal stress values during the deformation of the material [36]. For this reason, in previous studies [35,37], methods were developed to compensate for the inaccuracy of computed microtomography in FEM calculations. Due to the characteristics of both these methods, the second method was used in this study [37], which takes into account the fissures between the sintered powder particles that are omitted in the microtomographic measurements. The numerical calculations included the non-linearity of the material and implemented the normalised Cockroft-Latham ductile fracture criterion [38], thus taking into account the fracture process of the material mesostructure, up to the macrofracture initiation. It should be emphasised that, in the available literature, no other studies describing the numerical modelling of the mesostructure deformation and fracture process taking into account the local fracture of porous metals using the Cockroft-Latham criterion and computed microtomography have been noted. The paper presents and analyses the results obtained from calculations in the form of nominal stress-strain curves, as well as stress and strain distributions in a deformed material, and the variability caused by the mesofracture process. Moreover, the influence of the local fracture process of the material (at the mesoscopic scale) on its properties at the macro scale is described.

2. Materials

For the investigation described in this work, porous sinters of 316L steel with various porosity values were used. Material specimens were made of 316L steel powder with a particle size of 125–250 μm. The sinters were obtained by powder metallurgy and, more specifically, by sintering with cold pressing. In the cold pressing process, three average pressures of 200 MPa, 400 MPa and 600 MPa were used, with which various porosities of the material were obtained, 41%, 33% and 26%, respectively. The investigated porous structures were mostly open cell. There are also single small closed pores in the structure resulting from the sintering production process. The production process of the porous sinters studied is described in more detail in the works of Grądzka-Dahlke [39] and Falkowska et al. [6]. Fig. 1 shows examples of the porous structures of the investigated materials.

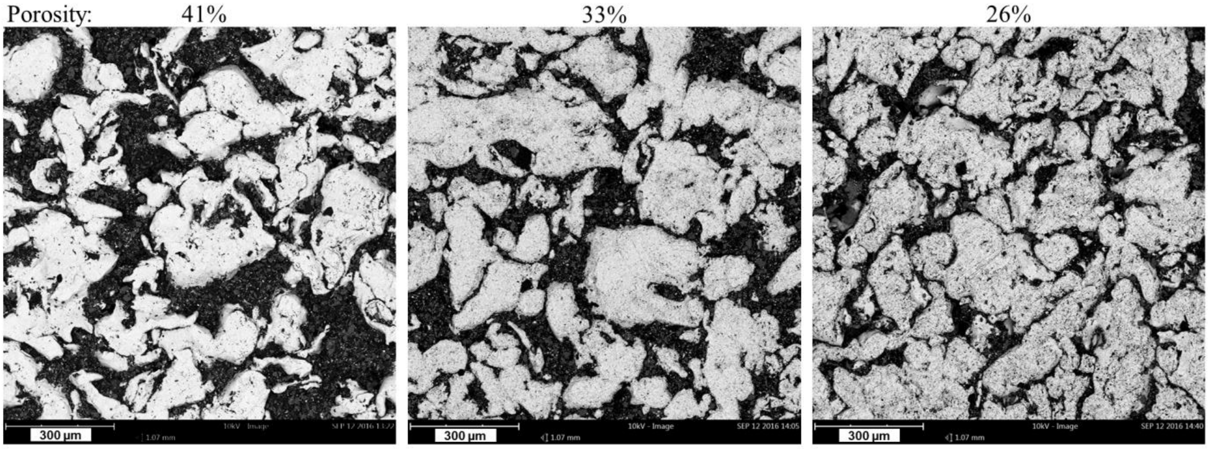

Fig. 1. Examples of porous structures of the investigated 316L steel sinters with a porosity of 41%, 33% and 26%.

3. Numerical modelling

For the numerical modelling of the fracture process described in the paper, a procedure consisting of the following stages was used (Fig. 2):

1) preparation of porous sinters for micro-CT imaging;
2) performing microtomographic measurements of the investigated porous structures;
3) processing and modification of microtomographic images in order to take into account the details of the geometry of the material mesostructure in the numerical modelling of the deformation and fracture process;
4) creating a spatial model of the porous mesostructure of the studied materials on the basis of modified images obtained by computed microtomography;
5) generating a spatial finite element mesh of the porous structure;
6) determination of the non-linearity of the solid material from which the powder for the production of porous material was obtained;
7) application of the material fracture criterion in the calculation model (on the level of the finite element);
8) numerical modelling of stress and strain fields using FEM, taking into account the local fracture of the mesostructure.

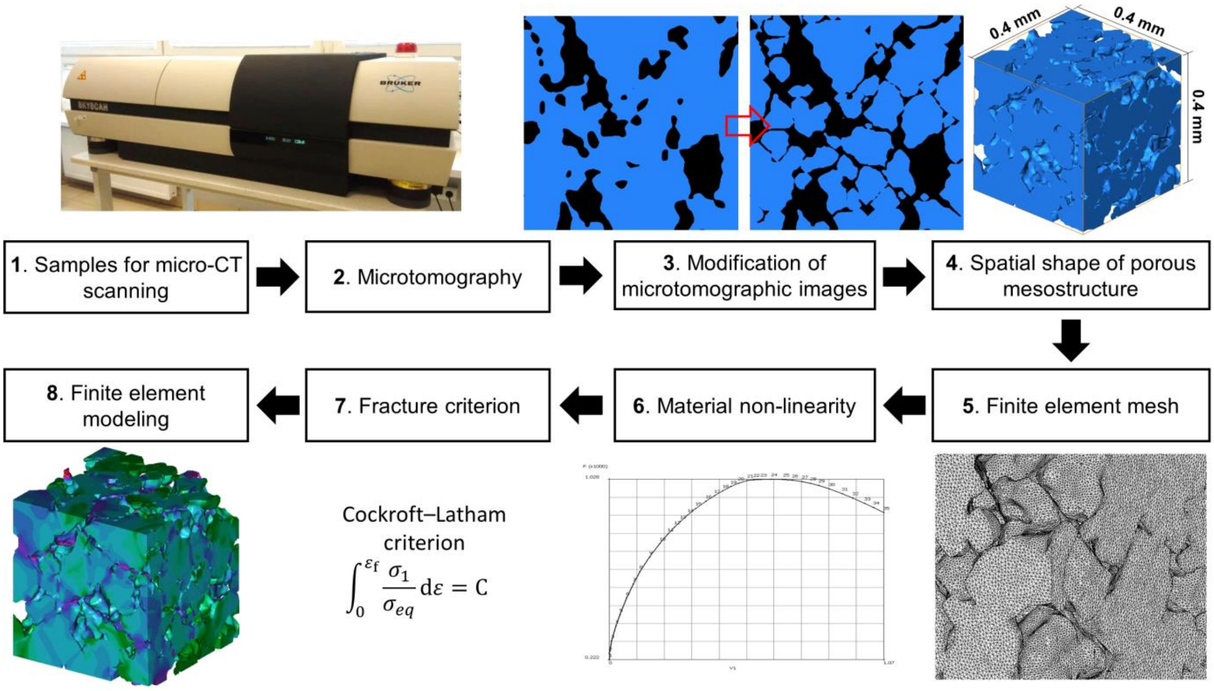

Fig. 2. The procedure for numerical modelling of the fracture process of porous metals with the use of computer microtomography.

3.1. Mapping the shape of the material mesostructure based on microtomographic images

In order to recreate the shape of the mesostructure of the investigated porous sinters, computed microtomography was used. The tomographic measurements were made using a high-resolution micro-CT Bruker SkyScan 1172. Using the SkyScan 1172 device and other similar micro-CT devices, the size limitations of the tested objects strongly depend on the assumed measurement accuracy (pixel size). With an accuracy such as that described in this paper (pixel size approx. 3 μm), the maximum size of the object is 12 x 8 mm. As the measurement accuracy decreases, objects can be tested up to a maximum diameter of about 5 cm. The microtomographic scanning performed allowed us to obtain reconstructed images of material cross-sections with a single pixel size of 2.91 μm. The measurement parameters were described in the previous work by Doroszko and Seweryn [35]. The accuracy of the microtomographic measurement obtained is insufficient to recreate the details of the porous structure, such as the fissures between the particles of sintered steel powder and small pores, with a size below the scanning accuracy (Fig. 1). The lack of mapping of these elements of the mesostructure has a significant impact on the process of deformation and fracture of the material, as well as the values of stress and strain in the deformed material [24,37,40]. For this reason, a method to compensate for the inaccuracy of microtomographic measurement in numerical calculations was used to model the mesofracture process of porous 316L steel sinters. This method consists of modifying tomographic cross-sections by applying a sequence of image processing operations in order to generate the geometric shape of the fissures between the sintered powder particles, omitted in the micro-CT measurements [37]. The modification method is based mainly on image processing using watershed segmentation [41]. In watershed segmentation, each two-dimensional grayscale image can be represented as a three-dimensional geological map (with a specific topology) in which the pixels with the highest value (e.g. obtained from a distance transform) are the vertices. The pixels with the lowest value, on the other hand, form valleys on the relief map. The watershed algorithm using markers requires two input images. The first is the image that will be processed to define the watershed lines (object separation lines). The second image contains markers (H-maxima), i.e. areas indicating the center of flooding. The areas are flooded starting from the markers towards increasing pixel values. In places between the flooded areas (on their borders) there are local maximum pixel values. The combination of these pixels creates dividing lines, separating flooded areas. It is also worth noting that image processing operations are constantly developed in order to improve the mesostructure mapping of materials [42]. The modification procedure of the tomographic cross-sections used consisted of the following stages (Fig. 3):

1) Increasing the resolution of microtomographic images - to obtain smaller pixels. In the next image processing operations, it will allow to increase the detailed mapping of the studied mesostructures shape.
2) Filtering the images with a Gaussian filter - to increase the homogenization and smoothing of images.
3) Binarisation (thresholding) - separation of pixels representing the solid material from the images in the entire volume of the porous sinter.
4) Separation of mesostructure objects (particles) based on the watershed algorithm - the particles of the porous structure are separated based on the topology of the images represented by the various shades of gray of the pixels.
5) Morphological opening operation in order to deepen the fissures between separated particles. The use of a morphological opening operation enables the mapping of the gaps shape occurs in this type of material. The gaps are wider on the surface and taper into the material.
6) Filtering the images with a majority filter to partially blur the separation lines and to shape the fissures between the particles. The dividing lines between the particles are removed and the particles are connected deeper within the structure.

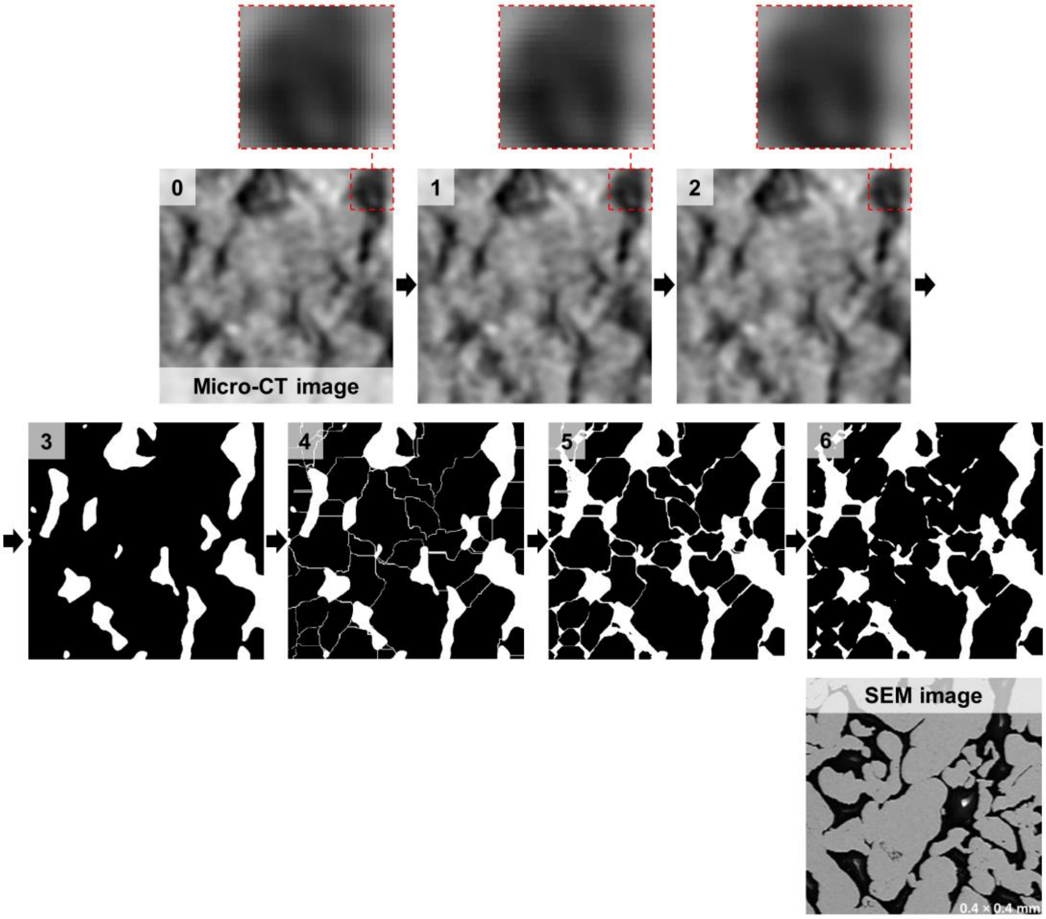

Fig. 3. Diagram of the process of modifying microtomography images using image processing operations [37] and a comparison to an exemplary cross-section of a material with a porosity of 41% obtained by SEM [39].

Figure 3 also shows an example of a cross-sectional view of 316L steel with a porosity of 41% obtained with a scanning electron microscope (SEM). The cross-section that does not take into account the modifications is shown in point 3 in Fig. 3. As can be seen, its shape is qualitatively significantly different from the cross-section shape obtained by SEM. This is due to the insufficient accuracy of the micro-CT device. On the other hand, the method developed in Doroszko and Seweryn [37] allows for taking into account a significant part of the details omitted as a result of microtomographic measurements. Based on the modified tomographic cross-sections, three cube-shaped three-dimensional geometric models (with dimensions 0.4 × 0.4 × 0.4 mm) were generated, one for each of the tested material porosities. Cross-section modification and generation of geometric models were carried out using Thermo Scientific Avizo 9.7.0 software. In order to create 3D models, a widely used procedure of 3D geometry reconstruction based on tomographic images was used. The main steps in such a procedure are as follows:

1) Arranging the sections in the correct order with an appropriate spacing between them resulting from microtomographic measurements.
2) Marking in the images of pixels with shades of gray corresponding to the geometry of the solid material in the sample (thresholding).
3) Building a three-dimensional model by generating and connecting voxels (the volumetric equivalent of a pixel) based on previously marked pixels.
4) Model surface triangulation.

The generated geometric models were then exported in the form of surface finite element meshes.

3.2. Numerical modelling of the fracture process of the mesostructure of porous material

A workstation equipped with Intel Core i9-7940X CPU, SSD M.2 NVMe drive and 64GB DDR4 memory was used for numerical calculations. Numerical modelling of the fracture process of the studied porous sinters was performed with the use of nonlinear calculation software (MSC.Marc) using a finite element method. The previously generated geometric models were imported into FEM software in the form of surface finite element meshes. Then, based on the surface meshes, solid finite element meshes were generated. Four-node tetrahedral solid finite elements of Tetra 134 type [43] were used for numerical calculations. The average size of the finite elements was approximately 0.003 mm. The individual mesostructures were divided into approximately 7.1, 9.2 and 8.4 million finite elements for the material porosity of 41%, 33% and 26%, respectively. Fig. 4 shows the structures of the investigated sintered 316L, divided into finite elements.

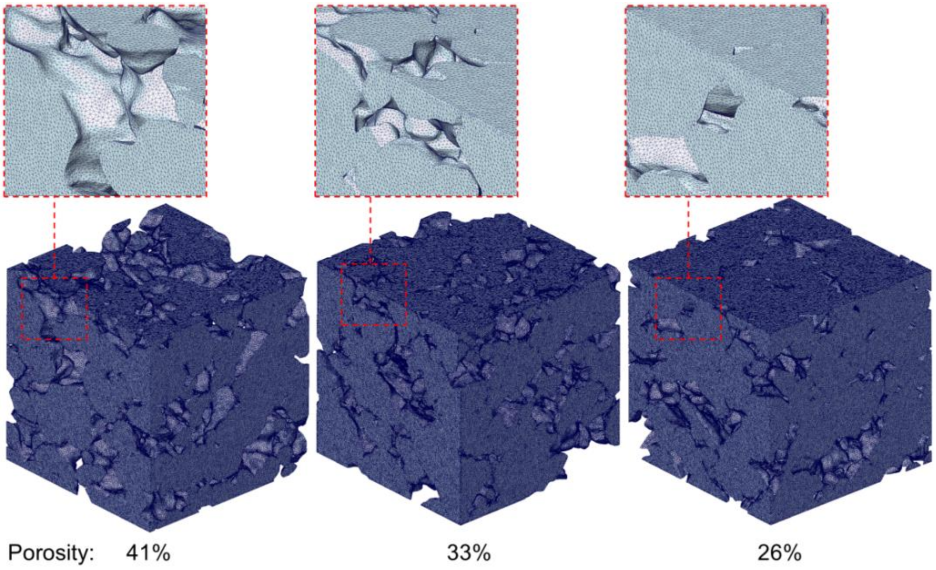

Fig. 4. Division of sintered mesostructures into finite elements with porosities of 41%, 33% and 26%.

In this work, the process of deformation and fracture of the mesostructure of porous metals was modelled during macroscopic tension of the material. In the described research, symmetric boundary conditions were used on three side walls of FEM models by applying zero nodal displacements to them in a direction normal to a given plane. The use of symmetric boundary conditions resulted in an eightfold increase in the volume of the mesostructure in numerical modelling. The tension of the models of porous mesostructures was carried out by assigning nodal displacements of the upper wall of the studied model in the direction of positive z-axis values of the coordinate system (Fig. 5).

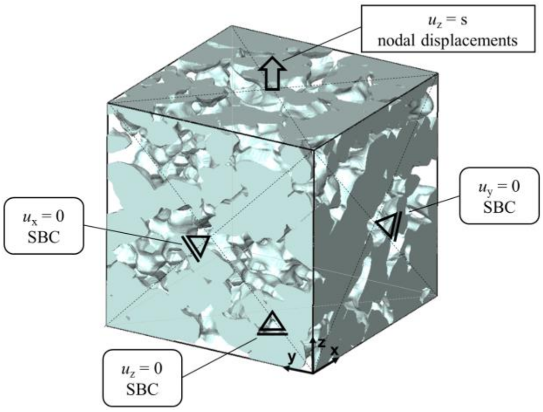

Fig. 5. Boundary conditions used for numerical modelling of the tension process of the investigated porous mesostructures.

For the numerical modelling of the deformation process, taking into account the local fracture of the material, an elasto-plastic material model with an implemented fracture criterion was used. The calculations assumed Young's modulus E_s = 202 GPa and Poisson's ratio ν_s = 0.3, obtained as a result of experimental tensile tests of solid 316L steel. The behaviour of the material under load in the range of plastic strain was defined by the true stress-strain curve (Fig. 6) and the application of the Huber-von Mises yield criterion. Bulk material non-linearity in the porous materials was determined using the hybrid method (experimental-numerical), based on the results of an experimental tensile test of solid 316L steel [35]. The true stress-strain curve of the solid 316L was obtained iteratively. Initially, the nominal stress-strain curve obtained from the experimental tests was used as the nonlinearity of the material in the numerical calculations. After the calculations, the convergence of the force-displacement curves obtained numerically and experimentally was checked, and then the true stress-strain curve was modified to improve their agreement. This sequence was repeated until the acceptable compliance of the nominal stress-strain curves obtained by experiment and calculations. Then, the true stress-strain curve was obtained at the center point of the specimen, i.e. at the point of the maximum stress and strain values location. The method used allowed us to take into account the necking effect of the tensile steel in the true stress-strain curve and the stress distribution in the most plastically deformed cross-section [44,45]. A more detailed description of the determination of the true stress-strain curve of the investigated solid 316L steel and a summary of the experimental and numerical tests are included in the work by Doroszko and Seweryn [35].

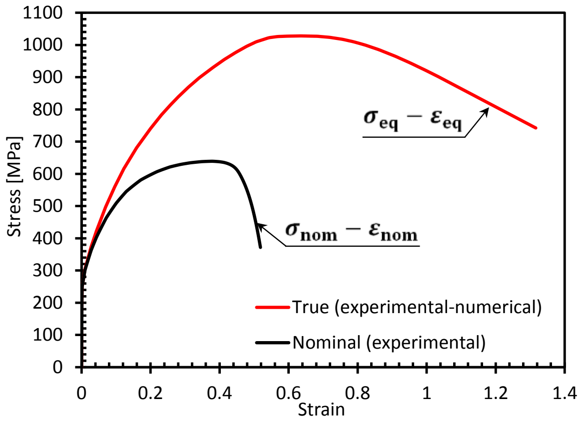

Fig. 6. The true and nominal stress-strain curve obtained for solid 316L steel and used in numerical calculations for porous sinters [35].

One of the most frequently used criteria in scientific research and engineering practice is the criterion proposed by Cockroft and Latham [46] and its modifications [38]. The reason for the frequent use of this criterion is its simple implementation in numerical calculations and the small number of constants to be determined on the basis of experimental data. In order to take into account the process of local fracture of the material as a result of its tension, the normalised Cockroft-Latham ductile fracture criterion implemented in the MSC.Marc software was used (at the finite element level), in the form [38]:

$$\int_0^{\varepsilon_\mathrm{f}} \frac{\sigma_1}{\sigma_\mathrm{eq}} \mathrm{d}\varepsilon^\mathrm{p} = C \tag{1}$$

where: σ_1 is the maximum principal stress in tension, σ_eq is the equivalent Huber-von Mises stress, ε^p is the equivalent plastic strain, ε_f is the equivalent plastic strain at fracture initiation moment, and C is the critical value parameter at which fracture initiation occurs. In the normalised ductile fracture criterion proposed by Cockroft and Latham, it was assumed that the fracture initiation in the material takes place at the moment of obtaining the critical value by the integral in Eq. (1). In order to determine this critical value, the relationship between the maximum stress values and plastic strain was used, obtained for a smooth tensile specimen made of solid 316L steel using the previously described experimental-numerical method. The value of the Cockroft-Latham criterion parameter at which the fracture initiation takes place was determined by calculating the integral from Eq. (1). The true values of stress and strain obtained as a result of FEM modelling were used for the calculations of this parameter. The values of stress and strain were determined in the center (in the axis) of the FE model, i.e. in the most plastically deformed place. The values of stress and strain in the model at the moment of initiating material fracture and the shape of true stress-strain curves are shown in the work of Doroszko and Seweryn [35]. The obtained critical value of the parameter causing the fracture initiation in the material was determined as $C = 1.297$. In order to simulate and visualise the fracture process of the mesostructure of the studied porous metals, the deactivation of finite elements was used. Finite elements in which the critical value of the implemented fracture criterion parameter was reached were deactivated.

4. Results

In this section, we present and discuss the numerical modelling results obtained for the deformation and fracture process at the mesoscopic scale. The nominal stress-strain curves obtained for the calculation model were compared with and without the implemented fracture criterion. The stress and strain distributions in the places of local fracture of the mesostructure were analysed and the results of the research were compared with the results of the experimental tests.

4.1. Tensile properties of the sintered 316L mesostructures

Based on the performed calculations, the macroscopic (effective) values of the strength properties of the investigated materials, such as Young's modulus, yield stress and maximum nominal stress, were determined (Tab. 1). Both in the case of the calculations with the implemented fracture model and without it, the same values of yield stress were obtained for the specific porosity of the material. This means that, until the macroscopic yield stress of the material was achieved, the critical value of the fracture criterion was not reached in the mesostructures of the studied sinters. However, in the case of the maximum nominal stress, the use of the fracture criterion in numerical calculations significantly reduced its value and brought it closer to the values obtained experimentally. Tab. 2 shows the percentage errors for the calculated strength properties. The greatest discrepancy between Young's modulus and the yield stress was obtained for the material with a porosity of 26%, amounting to 15.37% and 11.51%, respectively. However, for the remaining materials, it was from 1 to 6%. The inclusion of the material fracture criterion in the numerical model allowed us to reduce the mean absolute percentage error (MAPE) calculated for the maximum nominal stress, by approximately 18%. The MAPE obtained for the Young's modulus and the yield stress for all porosities was 7.63% and 6.35%, respectively.

Table 1. Mechanical properties of the porous sintered 316L steel, calculated by the finite element method and obtained by experimental tests [46].

Material porosity [%]	Young's modulus E [GPa]			Yield strength $R_{y0.2}$ [MPa]			Maximum nominal stress $\sigma_{\mathrm{nom}}^{\max}$ [MPa]		
	Exp.	No fracture	Fracture	Exp.	No fracture	Fracture	Exp.	No fracture	Fracture
41	32.9	33.4	33.4	47.0	43.9	43.9	58.2	71.1	62.5
33	53.2	56.4	56.4	74.2	73.5	73.5	110.5	134.9	112.8
26	72.2	61.1	61.1	106	93.8	93.8	175.9	198.1	169.5
0 (solid)	202	-	-	258	-	-	639	-	-

Table 2. Percentage errors of Young's modulus, yield strength and maximum nominal stress obtained using numerical calculations.

	Percentage error [%]			
Porosity [%]	Young's modulus E	Yield strength $R_{y0.2}$	Max nominal stress $\sigma_{\mathrm{nom}}^{\max}$	
	No fracture and Fracture	No fracture and Fracture	No fracture	Fracture
41	1.51	6.60	22.16	7.39
33	6.02	0.94	32.78	2.08
26	15.37	11.51	12.62	3.64

In Fig. 7 were compared the nominal stress-strain curves obtained by numerical calculations and experimental tests until the macroscopic failure of the material [47]. The presented graphs show the stress-strain curves obtained for four calculation variants: a model using a porous structure without geometry modification and without and with taking into account the fracture criterion (initial) [37]; a model with modification of geometry and without the fracture criterion; and a model taking into account the modification of the mesostructure geometry and the normalised Cockrotf-Latham criterion. The numerical curves present the stress-strain relationship until the maximum nominal strain determined based on experimental tests. The fact that there are slight discrepancies between the values of the maximum nominal strain calculated by FEM and on the basis of the experiment is the result of the use of the arc length method in numerical calculations, where a given calculation increment does not exactly hit the point determining the maximum nominal strain in the case of the experiment. At the moment of obtaining the maximum nominal strain using numerical calculations, the material macrocrack on the entire cross-section of the sample is not yet obtained. This may be due to the implementation of the crack criterion which does not take into account the complex stress state. All of the presented graphs show that the use of the modified Cockroft-Latham criterion in the computational model, and the deactivation of finite elements meeting this condition, resulted in a significant increase in the convergence of the numerical and experimental curves compared to the model taking into account only the elasto-plastic material model. It can also be concluded that the fracture of the material mesostructure, as a result of tension, has a large impact on the macroscopic hardening of porous 316L steel sinters. The best convergence of the numerical and experimental stress-strain curves was obtained for a material with a porosity of 26% with an implemented fracture criterion. The curves obtained for the modified models with the Cockroft-Latham criterion and under the experimental conditions indicate that the initiation of macroscopic fracture follows faster, i.e. it takes place at a lower nominal strain value for a material with a porosity of 41% than for a porosity of 33% and 26%

(Fig. 7). In order to determine the impact of modifying the shape of the porous structure, the curves obtained by the method using the modification of tomographic images and those without any modifications (initial model) were compared (Fig. 7). It can be seen that the use of the Cockroft-Latham fracture criterion in case of initial model causes a slight decrease in the value of the nominal tensile stress compared to the calculation models that do not take into account the fracture of the material. Comparing the results obtained using the initial model to the calculation models using modified tomographic images and to the results of the experiment, the nominal stress values are still significantly overestimated. This is due to the much larger cross-sections of the bridges connecting the mesostructure of the material, which failure at higher values of the nominal strain than in the case of the modified method. Smoother notches with a larger radius occurring in the mesostructures of initial model result in a lower stress concentration, and thus the smaller number of finite elements reaches the critical value of the implemented fracture criterion parameter.

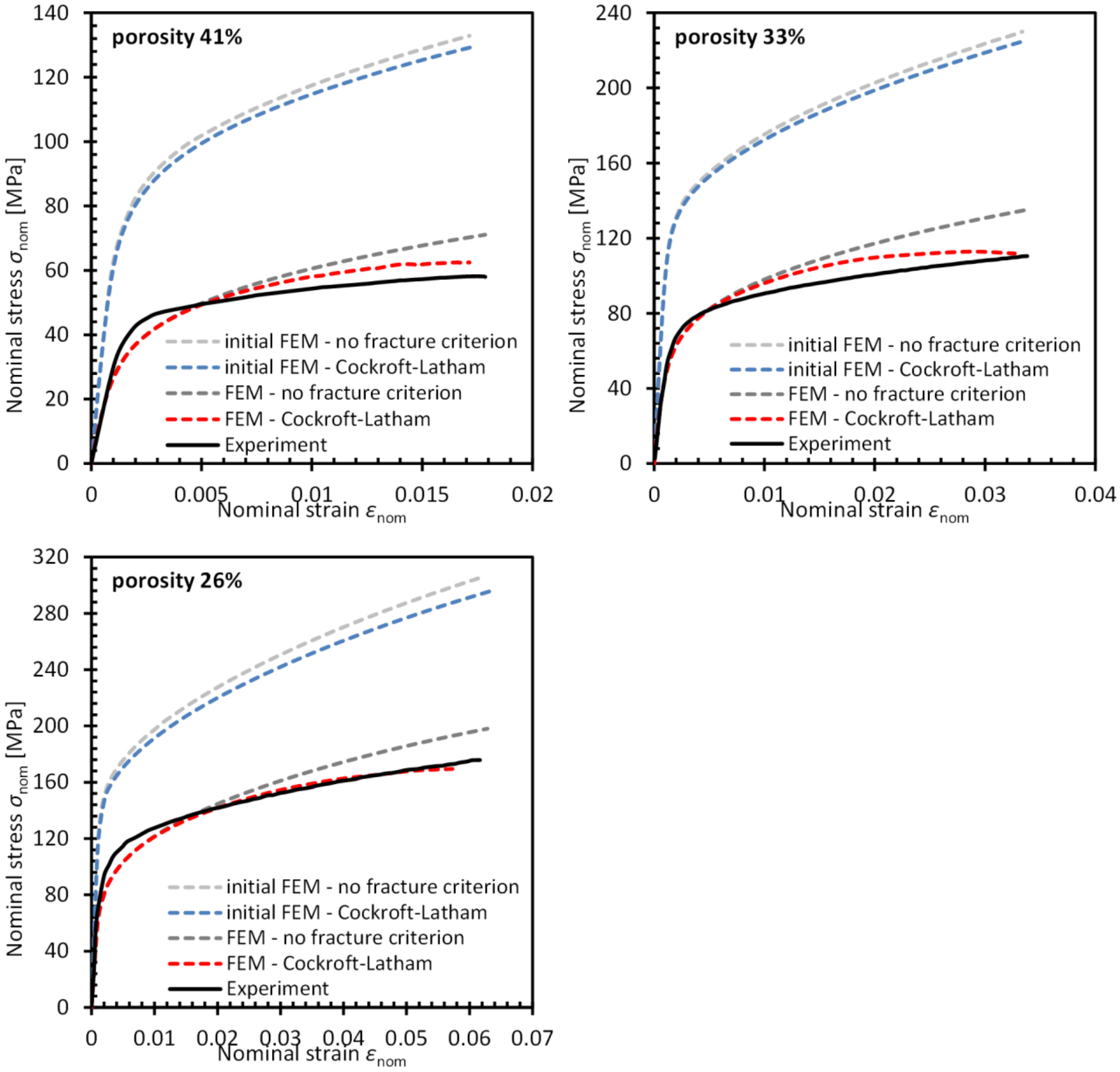

Fig. 7. Nominal stress-strain curves obtained for the investigated porous sintered 316L by means of numerical calculations and experimental tests [47].

4.2. Fracture process of porous mesostructures of sintered 316L steel

In the work by Falkowska et al. [6], the fracture process of tensile behaviour of porous 316L sinters was described on the basis of experimental tests, including microscopic analysis of the fracture surface (Fig. 8). At the beginning of loading, yielding and damage accumulation occur in the bridges between the sintered powder particles of the porous mesostructure. Microfracture initiation takes place at the edge of the pores or inclusions located in the area of the connection of the sintered powder particles. Further tension causes local fracture of the material by cracking the strongly plastically-deformed bridges connecting the individual particles of sintered powder. No cracks were observed inside the powder grains. The cracks then join together, which leads to cracking at the macro level. It has been shown that the fracture of the porous sinters tested in this paper, under conditions of monotonic uniaxial tension, is only ductile and inter-crystalline [6].

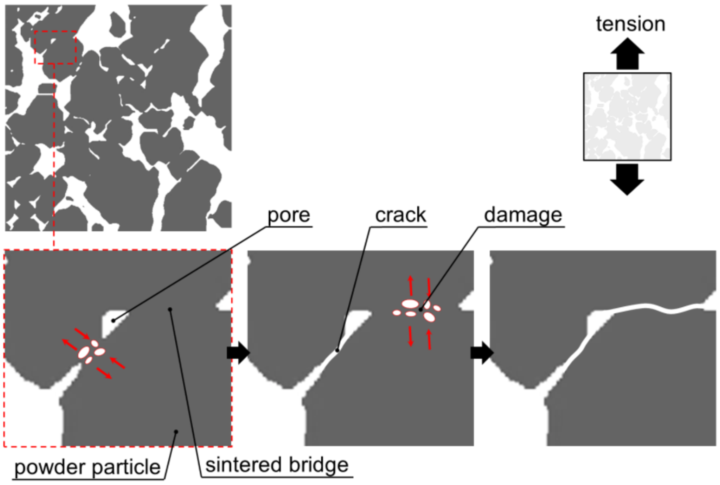

Fig. 8. The fracture process of porous sintered 316L steel during uniaxial tension (based on Falkowska et al. [47]).

As a result of the performed numerical calculations, the stress and strain distributions in the tensioned material in the z direction were also obtained. Figures 8, 9 and 10 show the equivalent stress distributions according to the Huber-von Mises hypothesis in the material with porosity of 41%, 33% and 26%, respectively (at the moment of obtaining the maximum value of macroscopic deformation $\varepsilon_{\mathrm{nom}}^{\mathrm{max}}$) and local fracture of the mesostructure during tension. As in the case of experimental studies in [47], it was observed that the fracture initiation of the studied porous metals takes place in the bridges connecting the sintered powder particles. There is also a high concentration of stress (according to the Huber-von Mises hypothesis) in these places. This is due to the small size of the cross-section of the bridges in relation to the remaining parts of the mesostructure and the shape of the notches (pores) with a small radius. It can be seen that, with a decrease in the porosity of the material, plastic zones with high values of strain and stress occupy a larger area of the sintered mesostructure (Fig. 9-11). The reasons for this are the higher number and the larger cross-section size of the bridges between the sintered powder particles (in less porous material), which bond the material together stronger and transmit a higher tensile load. The higher number of bridges and their larger cross-sectional area in the sinters with lower porosity are the result of the higher pressure in the material production process. In Fig. 9 to 11, the fracture trajectories resulting from tension are also indicated by red lines. In the case of material porosity of 41%, fracture occurs mainly along one plane (Fig. 9), while in a sinter with a porosity of 26%, bands of adjacent cracks can be determined, which have a decisive influence on the strength and stiffness of the material at the macro level. Fig. 12 shows microscopic images of the side surfaces of the studied sinters after monotonic uniaxial tension tests. Images were obtained with a Digital Microscope Olympus DSX110, and the surface of the samples was ground before microscopic examination, to better visualise the cracks formed. As in the case of numerical calculations (Fig. 9-11), the microscopic images indicate that, with the decreasing porosity of the material, the length and thickness of cracks in the tested materials increases (Fig. 12).

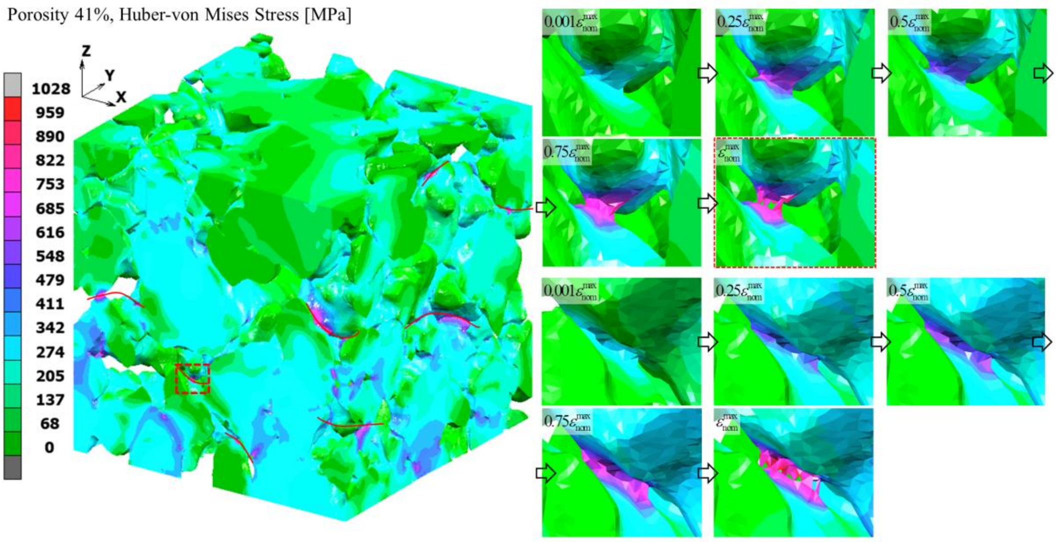

Fig. 9. Equivalent Huber-von Mises stress distribution in a material with a porosity of 41% at the moment of obtaining the maximum value of macroscopic strain $\varepsilon_{\mathrm{nom}}^{\mathrm{max}}$ (on the left) and local tensile fracture of the mesostructure (on the right).

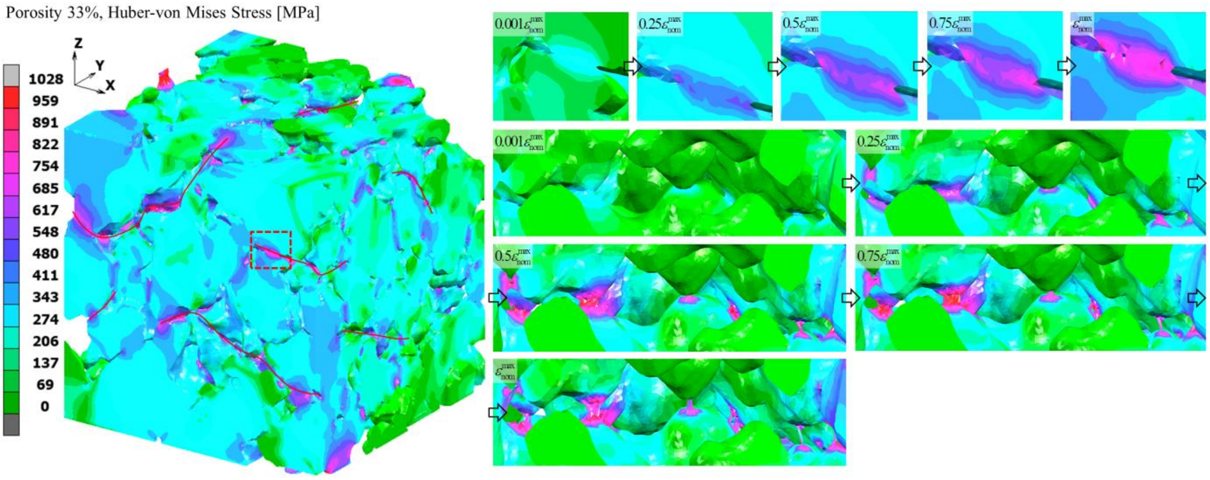

Fig. 10. Equivalent Huber-von Mises stress distribution in a material with a porosity of 33% at the moment of obtaining the maximum value of macroscopic strain (on the left) and local tensile fracture of the mesostructure (on the right).

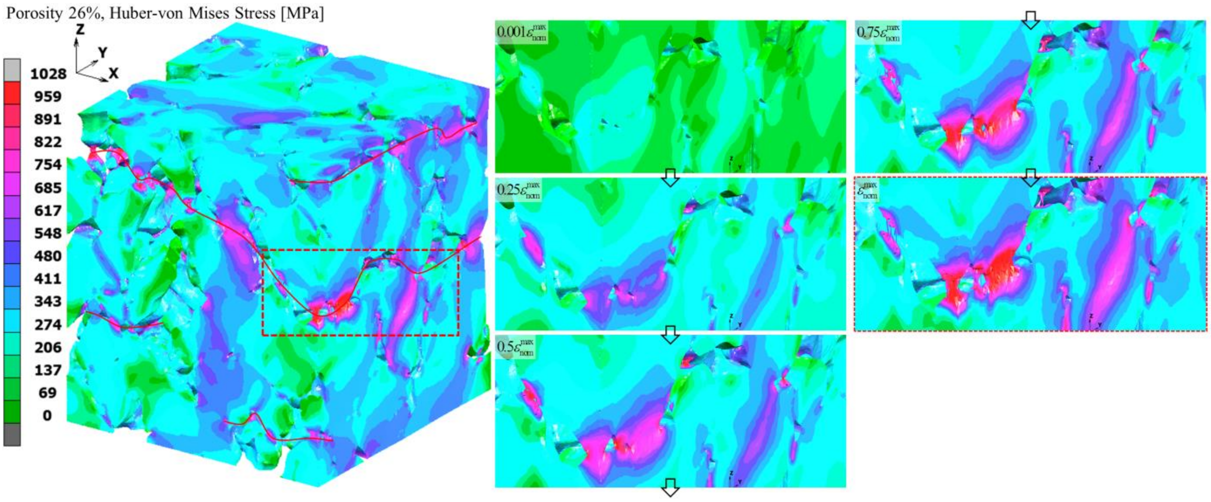

Fig. 11. Equivalent Huber-von Mises stress distribution in a material with a porosity of 26% at the moment of obtaining the maximum value of macroscopic strain $\varepsilon_{\text{nom}}^{\max}$ (on the left) and local tensile fracture of the mesostructure (on the right).

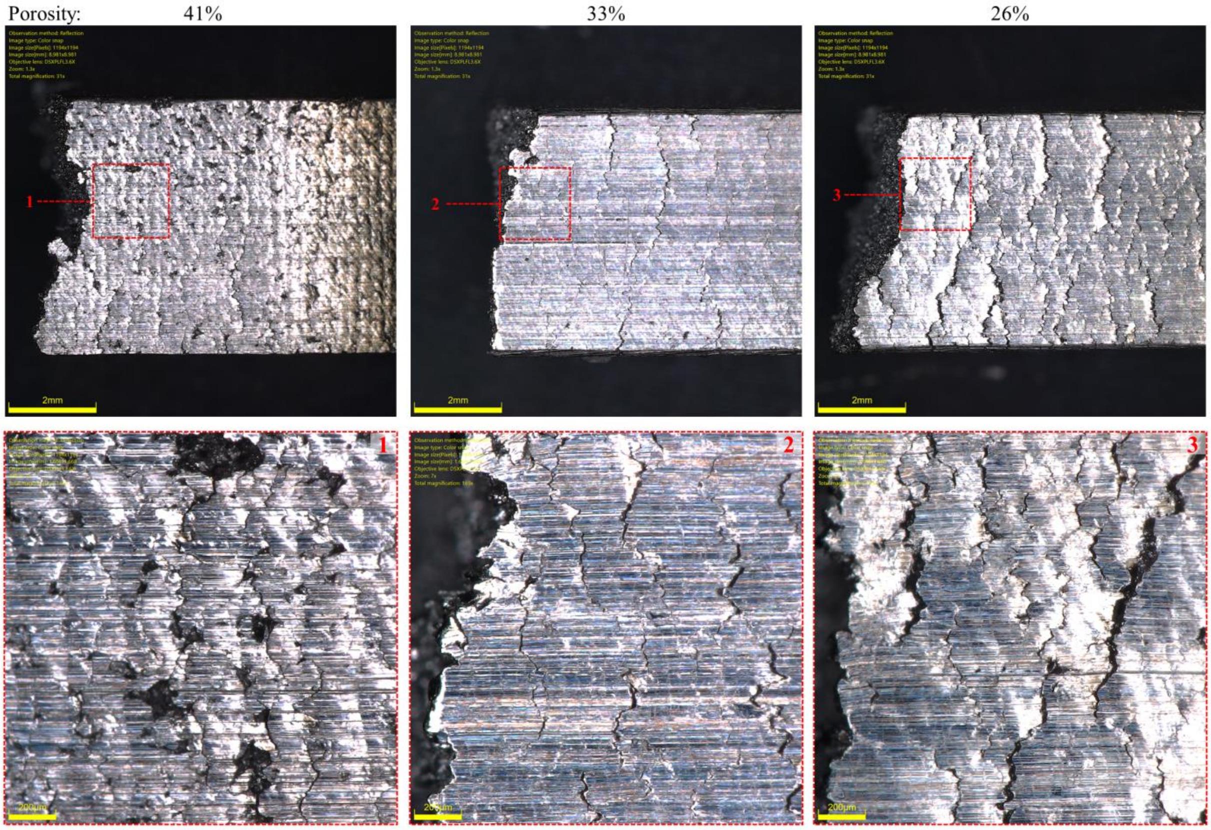

Fig. 12. View of the cracks on the side surface of the tested porous sinters obtained as a result of monotonic uniaxial tensile tests.

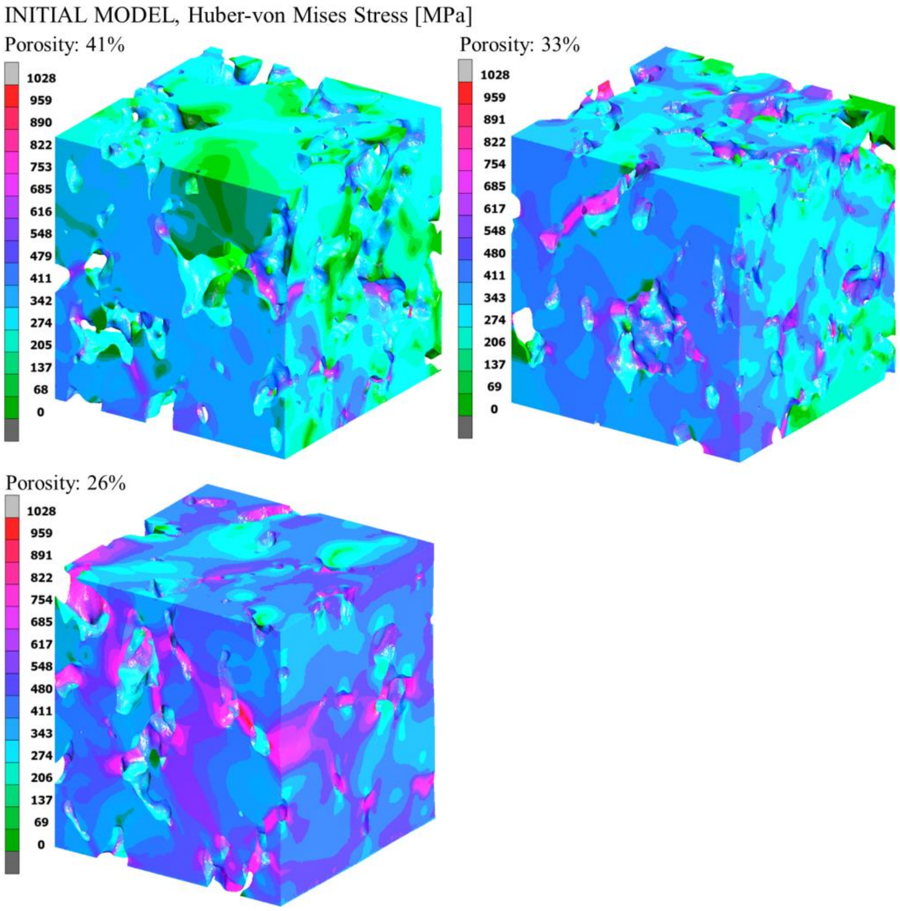

Fig. 13. Equivalent Huber-von Mises stress distribution in the initial model (without modification) with implemented fracture criterion at the moment of obtaining the maximum value of macroscopic strain $\varepsilon_{\mathrm{nom}}^{\max}$.

In Fig. 13 shown the equivalent stress distributions in the initial models at the moment of obtaining the maximum value of the nominal strain. As can be seen, the notches occurring in the studied mesostructures are smoother and have a larger radius than in the case of models using the modification of tomographic images. For this reason, there is less stress concentration in the bridges and notches, which leads to the occurrence of only a few local fracture locations in the material. The smaller number of fractured bridges than in the case of the modified models also causes a significant overestimation of the nominal stress value during the macroscopic deformation of the material (Fig. 7).

Figures 14 and 15 show the stress and strain distributions in the modified models at the moment of obtaining a macroscopic strain of 0.5%. In the maps of the maximum principal stress (Fig. 14), it can be seen that the highest stress values are in the bridges connecting the particles of the mesostructure. The stress values in these places reach comparable values. Whereas, with the decrease in the porosity of the material, the areas of the occurrence of the maximum principal stress values become larger. In the case of the highest porosity, these areas can be compared to points, while for the lowest porosity they form interconnected bands. The locations of the zones with the highest value of shear stress partially coincide with the locations of the maximum values of the maximum principal stress. Figure 15 shows the maps of the equivalent plastic strain and the maximum shear strain. Equivalent plastic strain in the most deformed places reaches the highest values in similar places as the maximum values of the principal stress. The maps of the maximum principal strain were very similar to the maps of the equivalent plastic strain, therefore they are not included in the figure. Based on the analysis of the maximum shear strain distributions (Fig. 15), it can be observed that the places of their maximum values coincide with the places of the maximum values of the equivalent plastic strain. Whereas, the maximum values in the bridges increase with the value of the material porosity. The strain distributions do not show a significant dominance of the maximum principal strain over the maximum shear strain in the most plastically deformed places.

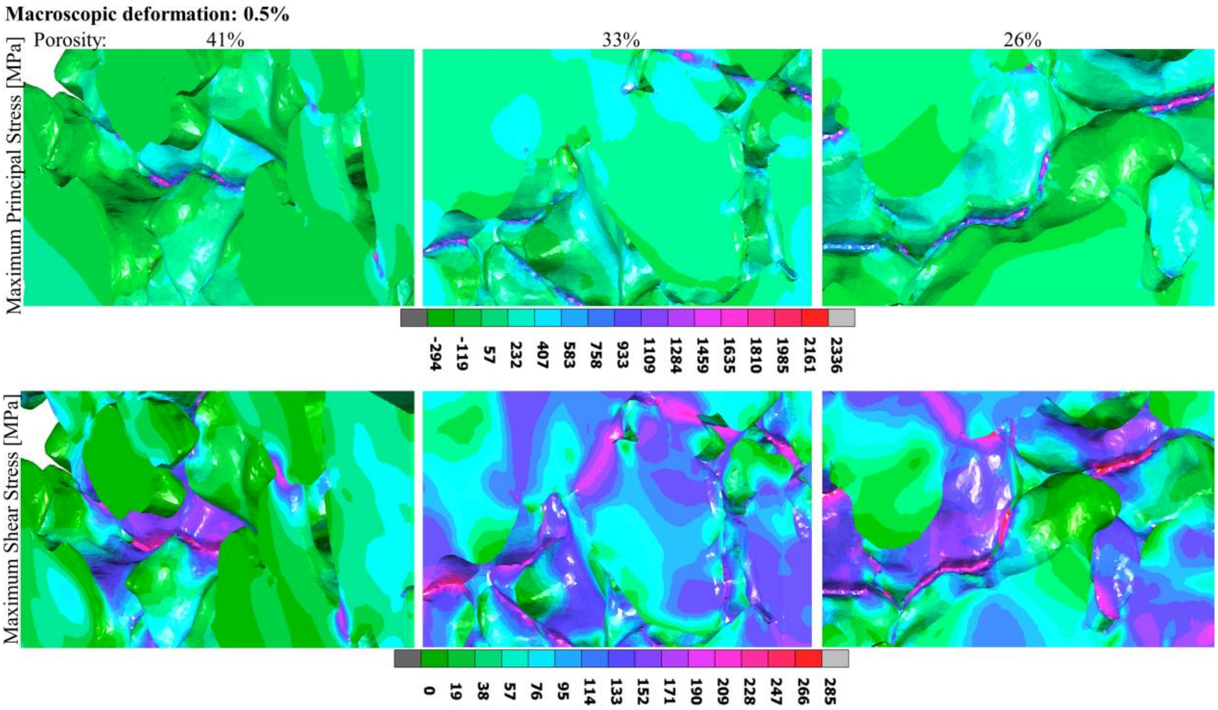

Fig. 14. Distributions of maximum principal stress (on top) and maximum shear stress (on bottom), at the moment of reaching the macroscopic strain 0.5%.

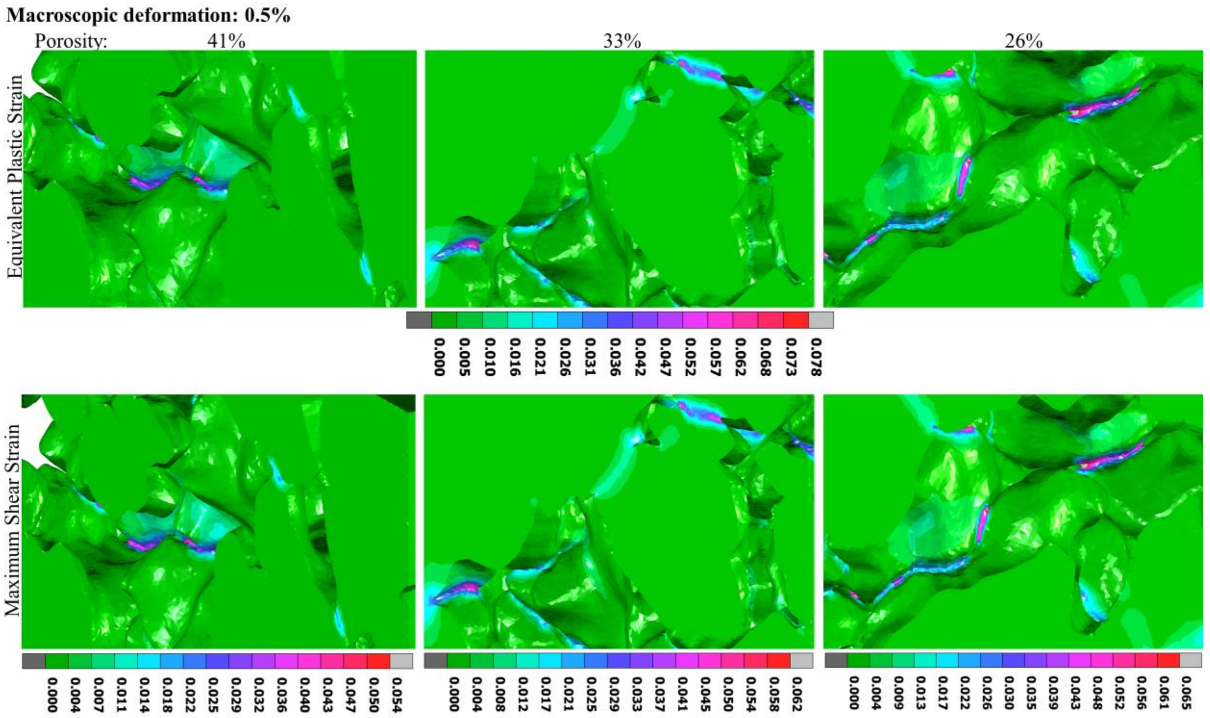

Fig. 15. Distributions of equivalent plastic strain (on top) and maximum shear strain (on bottom), at the moment of reaching the macroscopic strain 0.5%.

Figures 16 and 17 show the stress and strain distributions in the modified models at the places of material mesofracture, respectively, at the moment of obtaining the maximum value of macroscopic strain $\varepsilon_{\mathrm{nom}}^{\mathrm{max}}$. In Fig. 16, it can be seen that, with the increase in porosity of the material, the gradient of the maximum principal stress value decreases in the most plastically deformed places. However, the maximum shear stress locally (in the most plastically deformed places) reaches comparable maximum values for all of the mesostructures studied. This means that as the porosity of the material decreases, the maximum principal stress has an increasing influence on the fracture initiation. It can also be seen that at the time of macroscopic fracture initiation, as the porosity of the material decreases, there is a noticeable increase in the areas dominated by the maximum principal stress (Fig. 16). Fig. 17 shows that for a material with 41% porosity, the maximum deformation values at the moment of obtaining the maximum experimental macroscopic stress value $\varepsilon_{\mathrm{nom}}^{\mathrm{max}}$ are significantly lower (more than 2 times) than for the remaining sinters. This is due to a much lower nominal strain obtained in the experiment, as well as higher number of local cracks for material with the lowest value of effective modulus of elasticity. The maximum values of strain increase with the decrease in porosity, which is caused by the longer deformation time until the maximum value of the macroscopic strain $\varepsilon_{\mathrm{nom}}^{\mathrm{max}}$.

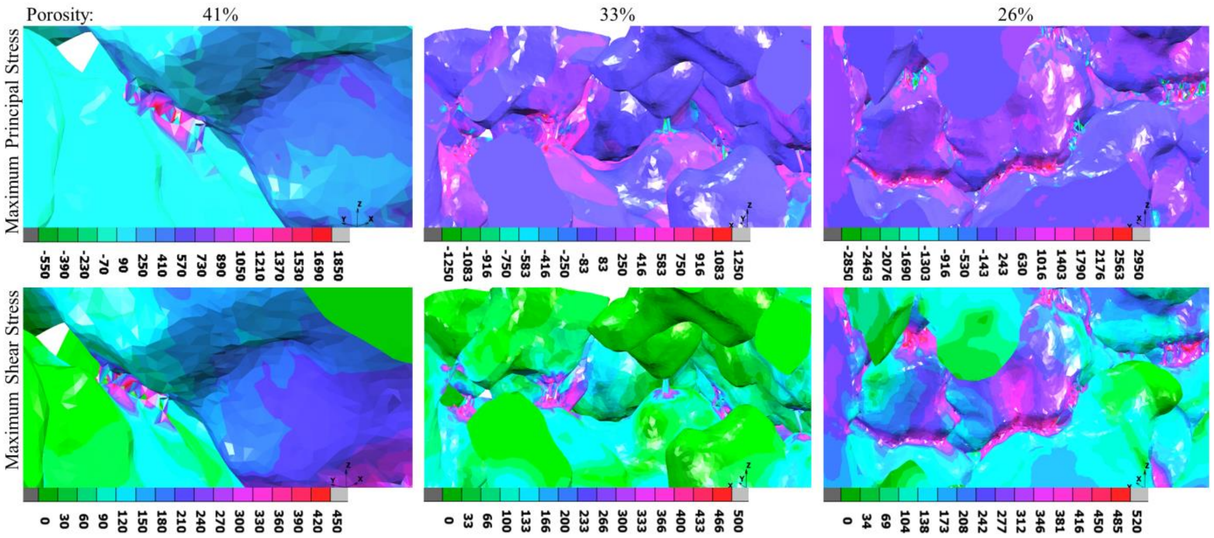

Fig. 16. Stress distributions in the mesofracture locations at the moment of obtaining the maximum value of macroscopic strain $\varepsilon_{\mathrm{nom}}^{\max}$.

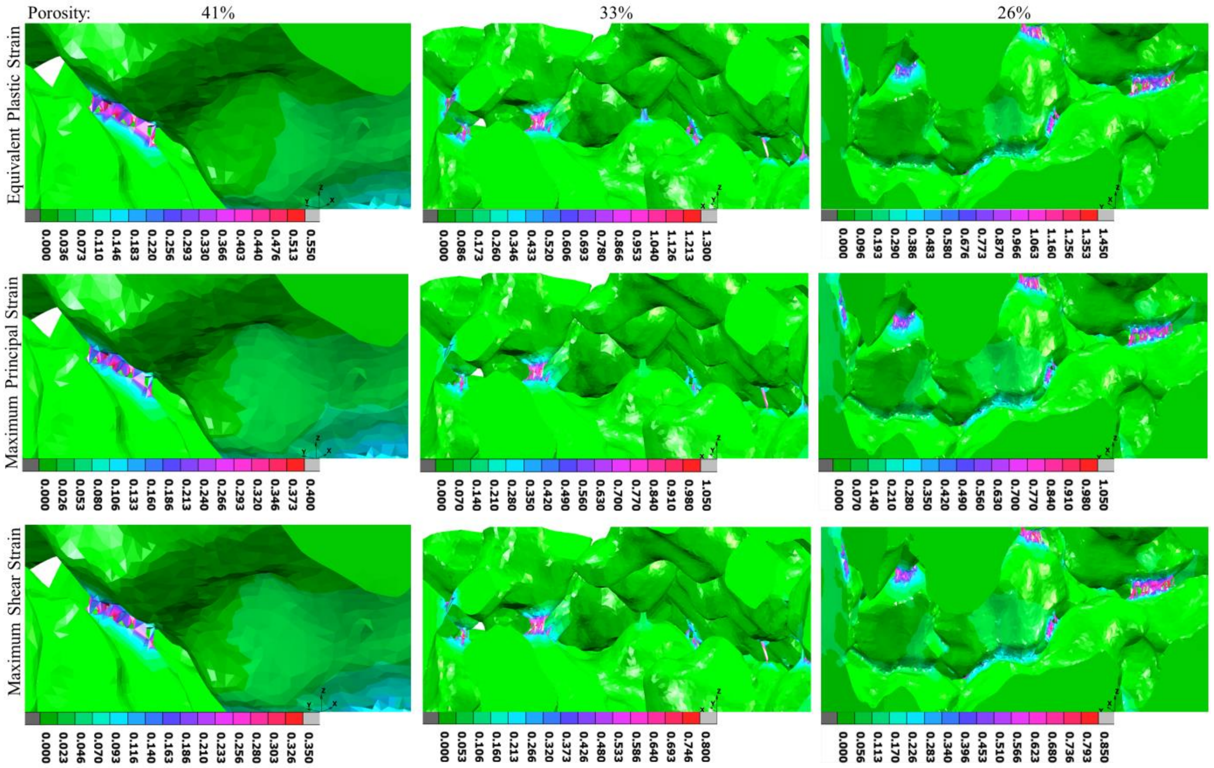

Fig. 17. Strain distributions in the mesofracture locations at the moment of obtaining the maximum value of macroscopic strain $\varepsilon_{\mathrm{nom}}^{\max}$.

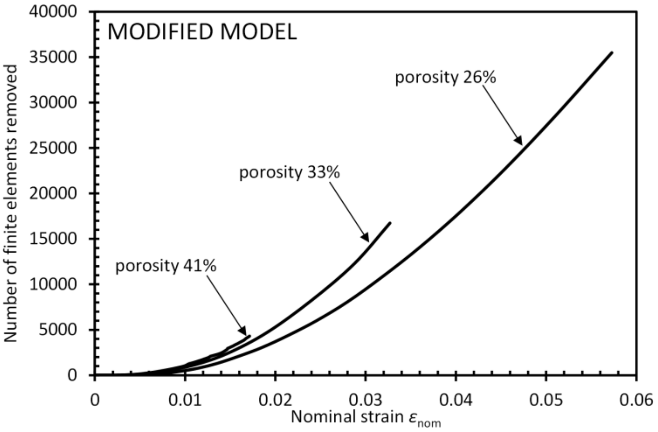

Fig. 18. The dependence of the number of deactivated finite elements on the value of the nominal strain during the tensile deformation obtained for modified models.

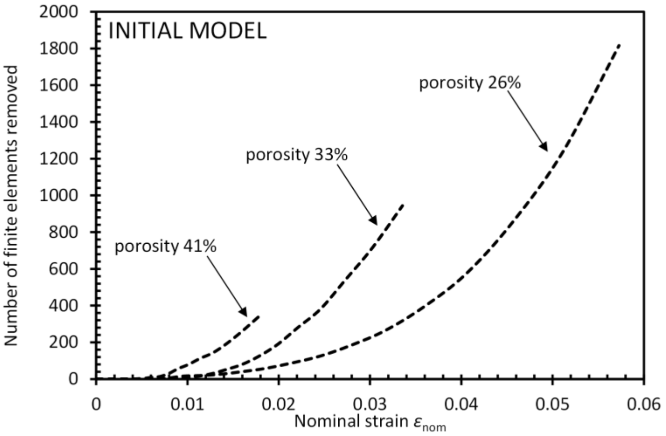

Fig. 19. The dependence of the number of deactivated finite elements on the value of the nominal strain during the tensile deformation obtained for initial models.

Fig. 18 shows the curves of the dependence of the number of deactivated finite elements (as a result of meeting the fracture criterion) on the nominal strain obtained for modified models with all of the studied material porosities. With the decrease in porosity, for the same value of nominal deformation, the number of finite elements that were deactivated as a result of reaching the assumed fracture condition decreases. This is due to the fact that the material with higher porosity has a smaller number of bridges in the mesostructure of the material. On the other hand, the intensity of deactivation of finite elements is related to the size of the cross-section of the connections between the sintered powder particles. In a sinter with a porosity of 26%, there are bridges with the largest cross-sections among the investigated materials and, therefore, they are slower to fracture than in sinters with higher porosity. In Fig. 19 shown the curves of the number of deactivated finite obtained for initial models. As can be seen, the shape of these curves is comparable to the curves obtained for the modified models. Whereas, the number of finite elements in which the critical value of the fracture criterion parameter has been reached is significantly lower than in the case of the modified models. At the moment of obtaining the maximum value of the nominal strain, it is 15-20 times less finite elements than in the case of the modified model (Fig. 18). This is due to the much larger cross-sections of the bridges connecting the mesostructure of the material, which failure at higher values of the nominal strain than in the case of the modified method. Smoother notches with a larger radius occurring in the mesostructures of initial model result in a lower stress concentration, and thus the smaller number of finite elements reaches the critical value of the implemented fracture criterion parameter. It should be noted that the size of the finite elements was similar for all three calculation cases, with different porosity. In order to develop the description of the damage-failure transition mechanism, it would be worth using an additional analysis of free energy release. The use of free energy release kinetics may complement the research presented in this paper and provide a valuable description of the multiscale fracture process of the porous materials [48,49].

5. Conclusions

This paper presents the procedure and results of modelling and numerical simulations (using the finite element method) of deformation and fracture processes occurring in the mesostructure of porous sinters of 316L steel under uniaxial tensile conditions. Due to the highly varied shape and size of the pores, the material has numerous stress and strain concentrations, as well as local plastic strain locations. The effect of their operation is the formation of local cracks (at the meso level) before the material reaches the limit state on the macro scale.

The implementation of the Cockroft-Latham ductile fracture criterion (modified by Oh et al. [38]) in finite element analysis, enables the simulation of the local fracture process by deactivating the elements in which the critical condition has been reached. Of course, it is then necessary to use a very dense mesh of division into finite elements. This approach gives good results (better compliance of the relationship between the nominal stress and the nominal strain) for the material tension. The performed numerical modelling correctly reflected the physical character of the tensile fracture of the material observed by microscopic examination. In the case of compression or shearing of the porous sintered metal alloys, it would be more reasonable to use the procedure of dividing the finite element into two, along the projected fracture plane. This procedure would significantly complicate the calculations and lengthen their time. When the Cockroft-Latham criterion [46] is applied, the plane of the projected fracture coincides with the plane on which the maximum normal stresses occur. Its use in conditions of a complex load state, where tension is not dominant, can lead to large discrepancies in the results of calculations and experimental tests. In further research, the implementation of the ductile fracture criterion, proposed and verified experimentally in the works by Derpeński and Seweryn [50], will be considered. However, this requires conducting experimental testing on specimens with notches made of solid material (from which the powder for sintering was made) under the conditions of tension and torsion.

The approach to modelling and numerical simulations using the finite element method of deformation and fracture of the porous 316L steel mesostructures presented in this paper can also be applied to other heterogeneous materials (composites in particular) or obtained by means of additive techniques. It is then important to determine, by means of experimental tests, the properties of the solid material (or individual components, in the case of composite materials), such as: elasticity constants, material hardening curve and critical values of normal and shear stress, as well as the effective properties of the heterogeneous material necessary to verify numerical calculations.

Nomenclature

C	critical value parameter of normalised Cockroft-Latham criterion
E	Young’s modulus of porous material
E_s	Young’s modulus of solid material
$R_{y0.2}$	Yield strength of porous material
s	Value of nodal displacements
u_x, u_y, u_z	Nodal displacements in the x-, y- and z- directions
ε_{eq}	True equivalent strain
ε_f	Equivalent plastic strain at fracture initiation moment
ε_{nom}	Nominal strain
ε_{nom}^{max}	Maximum nominal strain
ε^p	Equivalent plastic strain
ν_s	Poisson’s ratio of solid material
σ_1	Maximum principal stress
σ_{eq}	True equivalent stress
σ_{nom}	Nominal stress
σ_{nom}^{max}	Maximum nominal stress
FEM	Finite element method
MAPE	Mean absolute percentage error

Micro-CT	X-ray computed microtomography
SBC	Symmetric boundary conditions
SEM	Scanning electron microscope

Declaration of Competing Interest

The authors declare that they have no known competing financial interests or personal relationships that could have appeared to influence the work reported in this paper.

Acknowledgements

The paper was accomplished under grant no. UMO-2016/23/N/ST8/03519 at the Bialystok University of Technology and financed by the National Science Centre (Poland).

References

[1] Banhart J, Vinod-Kumar GS, Kamm PH, Neu TR, García-Moreno F. Light-metal foams: Some recent developments. Ciência Tecnol Dos Mater 2016;28:1–4. https://doi.org/10.1016/J.CTMAT.2016.06.002.

[2] Ashby M, Fleck N, Evans A, Wadley H, Delale F, Gibson L, et al. Metal Foams: A Design Guide. Appl Mech Rev 2002. https://doi.org/10.1115/1.1421119.

[3] Bolzoni L, Ruiz-Navas EM, Gordo E. Influence of sintering parameters on the properties of powder metallurgy Ti-3Al-2.5V alloy. Mater Charact 2013. https://doi.org/10.1016/j.matchar.2013.07.009.

[4] Orbulov IN, Szlancsik A, Kemény A, Kincses D. Compressive mechanical properties of low-cost, aluminium matrix syntactic foams. Compos Part A Appl Sci Manuf 2020;135:105923. https://doi.org/https://doi.org/10.1016/j.compositesa.2020.105923.

[5] Gradzka-Dahlke M, Dabrowski JR, Dabrowski B. Modification of mechanical properties of sintered implant materials on the base of Co-Cr-Mo alloy. J Mater Process Technol 2008. https://doi.org/10.1016/j.jmatprotec.2007.11.034.

[6] Falkowska A, Seweryn A, Tomczyk A. Fatigue life and strength of 316L sintered steel of varying porosity. Int J Fatigue 2018. https://doi.org/10.1016/j.ijfatigue.2018.02.023.

[7] Xie F, He X, Cao S, Qu X. Structural and mechanical characteristics of porous 316L stainless steel fabricated by indirect selective laser sintering. J Mater Process Technol 2013. https://doi.org/10.1016/j.jmatprotec.2012.12.014.

[8] Sharifnabi A, Fathi MH, Eftekhari Yekta B, Hossainalipour M. The structural and bio-corrosion barrier performance of Mg-substituted fluorapatite coating on 316L stainless steel human body implant. Appl Surf Sci 2014. https://doi.org/10.1016/j.apsusc.2013.10.029.

[9] Madej L. Digital/virtual microstructures in application to metals engineering – A review. Arch Civ Mech Eng 2017;17:839–54. https://doi.org/10.1016/J.ACME.2017.03.002.

[10] Zhang X, Jia G, Huang H. Numerical investigation of aluminum foam shield based on fractal theory and node-separation FEM. Chinese J Aeronaut 2011. https://doi.org/10.1016/S1000-9361(11)60086-1.

[11] Anoukou K, Brenner R, Hong F, Pellerin M, Danas K. Random distribution of polydisperse ellipsoidal inclusions and homogenization estimates for porous elastic materials. Comput Struct 2018. https://doi.org/10.1016/j.compstruc.2018.08.006.

[12] Liu T, Qin S, Zou D, Song W, Teng J. Mesoscopic modeling method of concrete based on statistical analysis of CT images. Constr Build Mater 2018;192:429–41. https://doi.org/10.1016/J.CONBUILDMAT.2018.10.136.

[13] Chavoshi SZ, Tagarielli VL, Shi Z, Lin J, Wang S, Jiang J, et al. Predictions of the Mechanical Response of Sintered FGH96 Powder Compacts. J Eng Mater Technol 2020. https://doi.org/10.1115/1.4045185.

[14] LI Z bin, LI X yan, ZHENG Y xuan. Biaxial mechanical behavior of closed-cell aluminum foam under combined shear—compression loading. Trans Nonferrous Met Soc China (English Ed 2020. https://doi.org/10.1016/S1003-6326(19)65178-2.

[15] Chawla N, Deng X. Microstructure and mechanical behavior of porous sintered steels. Mater Sci Eng A 2005. https://doi.org/10.1016/j.msea.2004.08.046.

[16] Deng X, Piotrowski GB, Williams JJ, Chawla N. Effect of porosity and tension-compression asymmetry on the Bauschinger effect in porous sintered steels. Int. J. Fatigue, 2005. https://doi.org/10.1016/j.ijfatigue.2005.06.041.

[17] Michailidis N, Stergioudi F, Omar H, Tsipas DN. An image-based reconstruction of the 3D geometry of an Al open-cell foam and FEM modeling of the material response. Mech Mater 2010;42:142–7. https://doi.org/10.1016/J.MECHMAT.2009.10.006.

[18] Zankel A, Wagner J, Poelt P. Serial sectioning methods for 3D investigations in materials science. Micron 2014;62:66–78. https://doi.org/10.1016/J.MICRON.2014.03.002.

[19] Rowenhorst DJ, Nguyen L, Murphy-Leonard AD, Fonda RW. Characterization of Microstructure in Additively Manufactured 316L using Automated Serial Sectioning. Curr Opin Solid State Mater Sci 2020. https://doi.org/10.1016/j.cossms.2020.100819.

[20] Luo G, Xue P, Sun S. Investigations on the yield behavior of metal foam under multiaxial loadings by an imaged-based mesoscopic model. Int J Mech Sci 2018. https://doi.org/10.1016/j.ijmecsci.2018.04.041.

[21] Madej L, Legwand A, Mojzeszko M, Chraponski J, Roskosz S, Cwajna J. Experimental and

numerical two- and three-dimensional investigation of porosity morphology of the sintered metallic material. Arch Civ Mech Eng 2018. https://doi.org/10.1016/j.acme.2018.06.007.

[22] Trawiński W, Tejchman J, Bobiński J. A three-dimensional meso-scale modelling of concrete fracture, based on cohesive elements and X-ray μCT images. Eng Fract Mech 2018. https://doi.org/10.1016/j.engfracmech.2017.10.003.

[23] Askari E, Cengiz IF, Alves JL, Henriques B, Flores P, Fredel MC, et al. Micro-CT based finite element modelling and experimental characterization of the compressive mechanical properties of 3-D zirconia scaffolds for bone tissue engineering. J Mech Behav Biomed Mater 2020. https://doi.org/10.1016/j.jmbbm.2019.103516.

[24] Doroszko M, Seweryn A. Pore-scale numerical modelling of large deformation behaviour of sintered porous metals under compression using computed microtomography. Mech Mater 2020. https://doi.org/10.1016/j.mechmat.2019.103259.

[25] Ghazi A, Berke P, Tiago C, Massart TJ. Computed tomography based modelling of the behaviour of closed cell metallic foams using a shell approximation. Mater Des 2020. https://doi.org/10.1016/j.matdes.2020.108866.

[26] Kashef S, Asgari A, Hilditch TB, Yan W, Goel VK, Hodgson PD. Fracture toughness of titanium foams for medical applications. Mater Sci Eng A 2010. https://doi.org/10.1016/j.msea.2010.08.044.

[27] Liu B, Wang XG, Tang Y, Yuan W, Fang C Bin, Wan ZP. Experimental Study on the Tensile Property of a Novel Oriented Linear Porous Metal. Adv Mater Sci Eng 2016. https://doi.org/10.1155/2016/3930703.

[28] Falkowska A, Seweryn A. Fatigue life of 316L steel sinters of varying porosity under conditions of uniaxial periodically variable loading at a fixed stress amplitude. Int J Fatigue 2018. https://doi.org/10.1016/j.ijfatigue.2018.07.025.

[29] Falkowska A, Seweryn A, Szusta J. Predicting the fatigue strength and life of 316L steel sinters of varying porosity for implants in a uniaxial loading state. Eng Fract Mech 2018. https://doi.org/10.1016/j.engfracmech.2018.07.030.

[30] Shevtsova L, Mali V, Bataev A, Anisimov A, Dudina D. Microstructure and mechanical properties of materials obtained by spark plasma sintering of Ni3Al–Ni powder mixtures. Mater Sci Eng A 2020. https://doi.org/10.1016/j.msea.2019.138882.

[31] Kaya AC, Zaslansky P, Nikolaus A, Fleck C. Tensile failure observations in sintered steel foam struts revealed by sub-micron contrast-enhanced microtomography. Mater Des 2016. https://doi.org/10.1016/j.matdes.2016.05.069.

[32] Perzyński K, Wrożyna A, Kuziak R, Legwand A, Madej L. Development and validation of multi scale failure model for dual phase steels. Finite Elem Anal Des 2017. https://doi.org/10.1016/j.finel.2016.10.001.

[33] Talebi S, Sadighi M, Aghdam MM, Mirbagheri SMH. Micro–macro analysis of closed-cell

aluminum foam with crushing behavior subjected to dynamic loadings. Mater Today Commun 2017. https://doi.org/10.1016/j.mtcomm.2017.10.004.

[34] Kozma I, Zsoldos I. CT-based tests and finite element simulation for failure analysis of syntactic foams. Eng Fail Anal 2019. https://doi.org/10.1016/j.engfailanal.2019.06.003.

[35] Doroszko M, Seweryn A. Numerical modeling of the tensile deformation process of sintered 316L based on microtomography of porous mesostructures. Mater Des 2015. https://doi.org/10.1016/j.matdes.2015.09.006.

[36] Doroszko M, Seweryn A. Modeling of the tension and compression behavior of sintered 316L using micro computed tomography. Acta Mech Autom 2015. https://doi.org/10.1515/ama-2015-0012.

[37] Doroszko M, Seweryn A. A new numerical modelling method for deformation behaviour of metallic porous materials using X-ray computed microtomography. Mater Sci Eng A 2017. https://doi.org/10.1016/j.msea.2017.02.055.

[38] Oh SI, Chen CC, Kobayashi S. Ductile fracture in axisymmetric extrusion and drawing: Part 2 workability in extrusion and drawing. J Manuf Sci Eng Trans ASME 1979. https://doi.org/10.1115/1.3439471.

[39] Gradzka-Dahlke M. Analysis of the processes occurring during compression of the porous 316L steel for biomedical applications. Maint Reliab 2010;4:16–22.

[40] Doroszko M, Seweryn A. Finite element modeling of anisotropic deformation behavior of the porous materials based on microtomographic images. AIP Conf. Proc., 2016. https://doi.org/10.1063/1.4965954.

[41] Beucher S, Lantuejoul C. Use of Watersheds in Contour Detection. Int Work Image Process Real-Time Edge Motion Detect 1979.

[42] Zhang J, Zhang Y, Wang G, Fang Q. The development of a 3D mesoscopic model of metallic foam based on an improved watershed algorithm. Model Simul Mater Sci Eng 2018. https://doi.org/10.1088/1361-651X/aab975.

[43] MSC Software Corporation, Marc® 2014.2, Product Documentation, Volume B: Element Library 2015.

[44] Tomczyk A, Seweryn A, Doroszko M. Monotonic behaviour of typical Al-Cu-Mg alloy pre-strained at elevated temperature. J Theor Appl Mech 2018. https://doi.org/10.15632/jtam-pl.56.4.1055.

[45] Doroszko M, Falkowska A, Seweryn A. Image-based numerical modeling of the tensile deformation behavior and mechanical properties of additive manufactured Ti–6Al–4V diamond lattice structures. Mater Sci Eng A 2021. https://doi.org/10.1016/j.msea.2021.141362.

[46] Cockcroft MG, Latham DJ. Ductility and the workability of metals. J Inst Met Inst Met 1968. https://doi.org/citeulike-article-id:4789874.

[47] Falkowska A, Seweryn A. Fatigue of sintered porous materials based on 316l stainless steel

under Uniaxial loading. Mater Sci 2015. https://doi.org/10.1007/s11003-015-9829-5.

[48] Naimark OB. Energy release rate and criticality of multiscale defects kinetics. Int J Fract 2016. https://doi.org/10.1007/s10704-016-0161-3.

[49] Naimark OB, Bayandin Y V., Zocher MA. Collective properties of defects, multiscale plasticity, and shock induced phenomena in solids. Phys Mesomech 2017. https://doi.org/10.1134/S1029959917010027.

[50] Derpenski L, Seweryn A. Ductile fracture of EN-AW 2024 aluminum alloy specimens with notches under biaxial loading. Part 2 – Numerical research and ductile fracture criterion. Theor Appl Fract Mech 2016. https://doi.org/10.1016/j.tafmec.2016.06.008.